Hierarchical MoS_2@NiFeCo-Mo(doped)-LDH Heterostructures as Efficient Alkaline Water Splitting (Photo)Electrocatalysts

Kayvan Moradi,[†,§] Maysam Ashrafi,[‡,¶,§] Abdollah Salimi,[*,‡,¶] and Marko M. Melander[*,†]

†*Department of Chemistry, Nanoscience Center, University of Jyväskylä, P.O. Box 35, FI-40014 Jyväskylä, Finland*

‡*Department of Chemistry, University of Kurdistan, Sanandaj, 66177-15175, Iran.*

¶*Research Center for Nanotechnology, University of Kurdistan, Sanandaj, 66177-15175, Iran.*

§*These authors contributed equally*

E-mail: absalimi@uok.ac.ir; marko.m.melander@jyu.fi

Abstract

Designing cost-effective electrocatalysts with fast reaction kinetics and high stability is an outstanding challenge that needs to be resolved to enable green hydrogen generation through overall water splitting (OWS). Layered double hydroxide (LDH) heterostructure materials are promising candidates to catalyze both oxygen evolution reaction (OER) and hydrogen evolution reaction (HER), the two half-cell reactions of OWS. This work develops a facile hydrothermal route to synthesize hierarchical heterostructure MoS_2@NiFeCo-Mo(doped)-LDH electrocatalysts, which exhibit extremely good OER and HER performance as witnessed by their low overpotentials of 178 mV

https://doi.org/10.26434/chemrxiv-2024-7cs2z **ORCID:** https://orcid.org/0000-0001-7111-1603

and 64 mV, respectively, at a current density of 10 mA cm^{-2} under light assistance. The MoS_2@NiFeCo-Mo(doped)-LDH‖MoS_2@NiFeCo-LDH OWS cell demonstrates a low cell voltage of 1.46 V at 10 mA cm^{-2} during light-assisted water electrolysis. The experimental and computational results demonstrate that doping of high-valence Mo atoms within and the deposition of MoS_2 quantum dots on the LDH matrix improves the electrocatalytic activity by 1) enhancing electron transfer, 2) making the electrocatalyst metallic, 3) increasing the number of active sites, 4) lowering the thermodynamic overpotential, and 5) changing the OER mechanism. Overall, the facile synthesis method enables the design of highly active MoS_2@NiFeCo-Mo(doped)-LDH heterostructure electrocatalysts.

Introduction

Modern societies are powered by fossil fuels but the extensive use of these resources has unintentionally caused substantial harm to our environment. In future, we need to cut down the carbon emissions and shift to renewable, clean, and sustainable energy technologies.[1–3] Green hydrogen produced through overall water splitting (OWS) catalysis has become the preferred choice due to its low of carbon emissions and high energy efficiency.[4] However, the production of hydrogen through water splitting relies on the use of noble metal electrocatalysts to achieve low overpotentials and rapid kinetics in the oxygen evolution (OER) and hydrogen evolution reactions (HER). Currently, the most successful commercial catalysts for OER and HER are based on noble metal oxides, such as IrO_2/RuO_2 and Pt-based compounds, respectively. However, their limited availability and high cost hinder their widespread use in large-scale applications. Hence, there is a large demand for cost-effective, stable, and efficient water splitting catalysts, which are made of earth-abundant elements and which exhibit low overpotentials and high reaction kinetics towards OER and HER.[5–9]

In the pursuit of more efficient OWS, a plethora of different types of transition-metal-based materials to catalyze OER and HER have been synthesized and designed over the past decade, including oxides,[10,11] sulfides,[12,13] borides,[14,15] phosphides,[16,17] carbides,[18,19] and nitrides,[20,21] as well as metal-organic frameworks (MOFs)[22,23] and layered double hydroxides (LDHs).[5,6,9,24] Besides new materials, it has also been shown that morphological control is an effective way of improving electrocatalytic activity. For instance, amorphous materials often exhibit increased electrocatalytic performance as compared to their crystalline counterparts due to structural and chemical disorder, the presence of defects, dangling bonds, and structural flexibility.[25,26] In general, the amorphization of crystalline materials has been viewed as a powerful way to improve HER and OER kinetics and the overall performance towards electrochemical water splitting.[25,26]

One realization of the combined material development and amorphization strategies is the design of transition metal-based LDHs, which have attracted considerable attention due to their high (photo)electrocatalytic activity for various reactions.[27–30] In particular, LDHs containing nickel (Ni), cobalt (Co), and iron (Fe) have exhibited very promising electrocatalytic performance, low overpotential, and long-term durability for the OER.[31–34] LDHs are, however, less used in the HER due to the weak hydrogen adsorption on these materials, which induces a substantial energy barrier for HER and consequently leads to sluggish water splitting kinetics.[35–37] Therefore, various physical and chemical strategies have been designed and explored to improve the catalytic properties of LDH, including morphology control[38,39] and the creation of defects and vacancies[40,41] Nevertheless, LDHs still encounter issues regarding sluggish reaction kinetics and slow mass transfer, a low concentration of electroactive sites, and limited electronic conductivity.[42–45]

The electrocatalytic activity of Ni/Fe/Co-LDHs remains constrained by two crucial factors: intrinsic reaction kinetics and mass transfer.[28,33,34,46] To overcome these issues, different catalyst design strategies have been employed. One approach involves the introduction of transition metal cations or non-metal atoms to modify the electronic structure, the presence of structural defects, and the local reaction or coordination environment at the LDH surface.[27,47–49] Additionally, the insertion of various anions or molecules between LDH layers can induce alteration in their the spacing, charge density, and hydrophilicity.[27,48,49] Another strategy entails controlling the mesoscopic structure through atomic vacancies or pores within the LDHs to increase their surface area, to expose more active sites, and to facilitate mass transfer.[27,48,49]

LDHs can also be interfaced and combined with other conductive materials or substrates to enhance their electrical conductivity and stability in a synergistic manner to boost the water splitting activity.[6,50] Some notable choices include metal clusters and molybdenum compounds, for instance.[3,37,48–52] The incorporation of 2D molybdenum sulfide (MoS_2) sheets, which are active HER electrocatalysts, has been shown to activate LDHs towards HER by introducing new active sites.[53,54] Moreover, as the electronic properties of MoS_2 nanostructures depend sensitively on their size, they have also been used to improve the (photo)electrocatalytic activity by introducing narrow and tunable band gaps.[51,55–59] The size- and morphology-dependent electronic structures[55,58,60] make the MoS_2 nanostructures highly appealing as co-catalysts for (photo)electrocatalytic HER.[51,55,59,61–64]

After carefully considering the above aspects, we hypothesized that 1) NiFeCo LDHs are an ideal materials class for OER, 2) the introduction of large, high-valance metal atoms (Mo) will lead to more pronounced amorphization of the LDH crystal structure, 3) the incorporating MoS_2 nanostructures on the LDH surface can enhance the HER (photo)electrocatalytic activity by introducing more HER active sites, and 4) the mass transfer, conductivity, and electrocatalytic active surface area to electroactive sites can be improved by depositing the catalyst material on a highly porous conducting substrate.

To test these hypotheses, we synthesized a series of hierarchical heterostructures of MoS_2@NiFeCo-Mo(doped)-LDH and MoS_2@NiFeCo-LDH using a straightforward hydrothermal method and electrodeposition approach on nickel foam (NF). The as-prepared catalyst MoS_2@NiFeCo-Mo(doped)-LDH demonstrated exceptional performance in HER and exhibited a low overpotential of 64 mV at 10 mA cm^{-2} under light illumination, which is lower than that of the benchmark Pt/C (91 mV). The MoS_2@NiFeCo-LDH electrodes exhibited very good OER performance and have a low overpotential of 178 mV at 10 mA cm^{-2} under light illumination, which is lower than that of the benchmark RuO_2 catalysts (327 mV) at 10 mA cm^{-2}. Furthermore, we used MoS_2@NiFeCo-Mo(doped)-LDH and MoS_2@NiFeCo-LDH as the HER and OER electrodes, respectively, in a two-electrode water-splitting system. This electrolytic cell was shown to be stable and to achieve a low cell voltage of 1.46 V for OWS at a current density of 10 mA cm^{-2}. Density functional theory (DFT) calculations allowed us to rationalize how and why each component of the complex, hierarchical LDH heterostructure contributes to the HER and OER activity. Overall, our work provides a facile and rational way to fabricate and design highly efficient and low-cost heterostructure catalysts for (photo)electrocatalytic water splitting. Given the modular synthesis approach of the LDH heterostructure, we expect that the design principles applied herein can be used for optimizing LDH-based electrocatalysts for various electrocatalytic processes.

Results and discussion

Structural Characterization

The LDH-heterostructures were synthesized under relatively mild conditions using a hydrothermal approach depicted in Figure 1a. In the first step, an LDH matrix with varying ratios of Ni, Fe, and Co (NiFeCo-LDH), and possibly doped with Mo (NiFeCo-Mo(doped)-LDH), was synthesized on a nickel foam (NF) substrate using a one-pot hydrothermal method. In the next step, MoS_2 QDs were immobilized on the LDH using a facile and rapid electrodeposition approach. The synthesis produces the self-supporting electrode materials of interest, MoS_2@NiFeCo-LDH and MoS_2@NiFeCo-Mo(doped)-LDH.

The surface morphology of the synthesized samples was examined using field-emission scanning electron microscopy (FE-SEM) and transmission electron microscopy (TEM). Figures 2a-d and Figures S1-2 present the FE-SEM images of the materials at various magnifications. The NiFeCo-LDH structure exhibits a flower-ball-like structure of uniformly grown ultrathin nanosheets (thickness 16-20 nm) on the NF(Figure 2a). Mo doping in NiFeCo-LDH resulted in thicker and denser nanosheets (thickness 18-24 nm) as shown in Figures 2b and S1. Moreover, Figures 2c, 2d, and S1 illustrate that the incorporation of MoS_2 QDs through electrodeposition onto the LDH host induces only minimal morphological changes in the underlying LDH. Further TEM analysis in Figures 2e-h shows that MoS_2 deposition leads to the formation of MoS_2 QDs on the LDH surface and does not lead to *e.g.* Mo-doping of the underlying LDH. The deposition of MoS_2 QDs onto NiFeCo-LDH and NiFeCo-Mo(doped)-LDH also reduces the LDH thickness (thickness 10-14 nm).

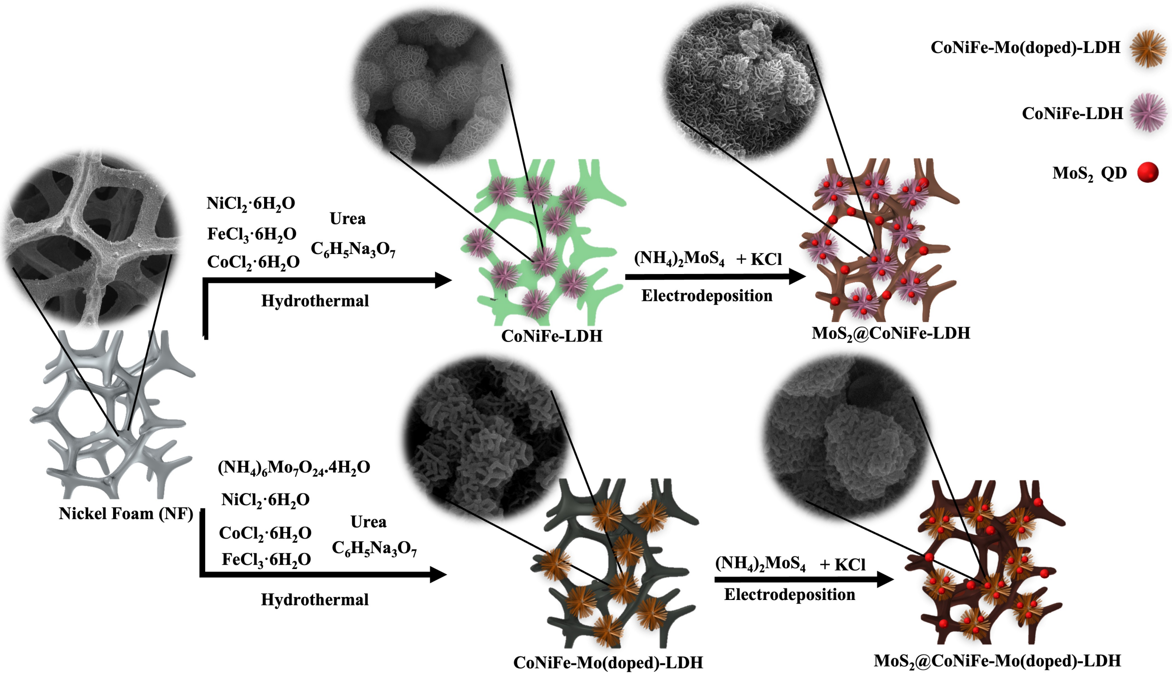

Figure 1: Schematic synthetic process of CoNiFe-LDH, CoNiFe-Mo(doped)-LDH, MoS_2@CoNiFe-LDH, and MoS_2@CoNiFe-Mo(doped)-LDH electrocatalysts on NF substrate.

The energy-dispersive X-ray spectroscopy (EDS) shows that all the deposited metals remain on the catalyst. This can be seen in the EDS spectra in Figure S3 which shows distinct elemental peaks corresponding to Ni, Co, Fe, Mo, S, and O in NiFeCo-LDH, NiFeCo-Mo(doped)-LDH, MoS_2@NiFeCo-LDH, and MoS_2@NiFeCo-Mo(doped)-LDH. Moreover, the SEM-EDS elemental mapping of MoS_2@NiFeCo-Mo(doped)-LDH validates the uniform distribution of constituent elements throughout the catalyst structure (Figure 2i). The SEM-

EDS maps for other heterostructures are presented in Figure S4 and affirm a uniform element distribution within the LDH structures.

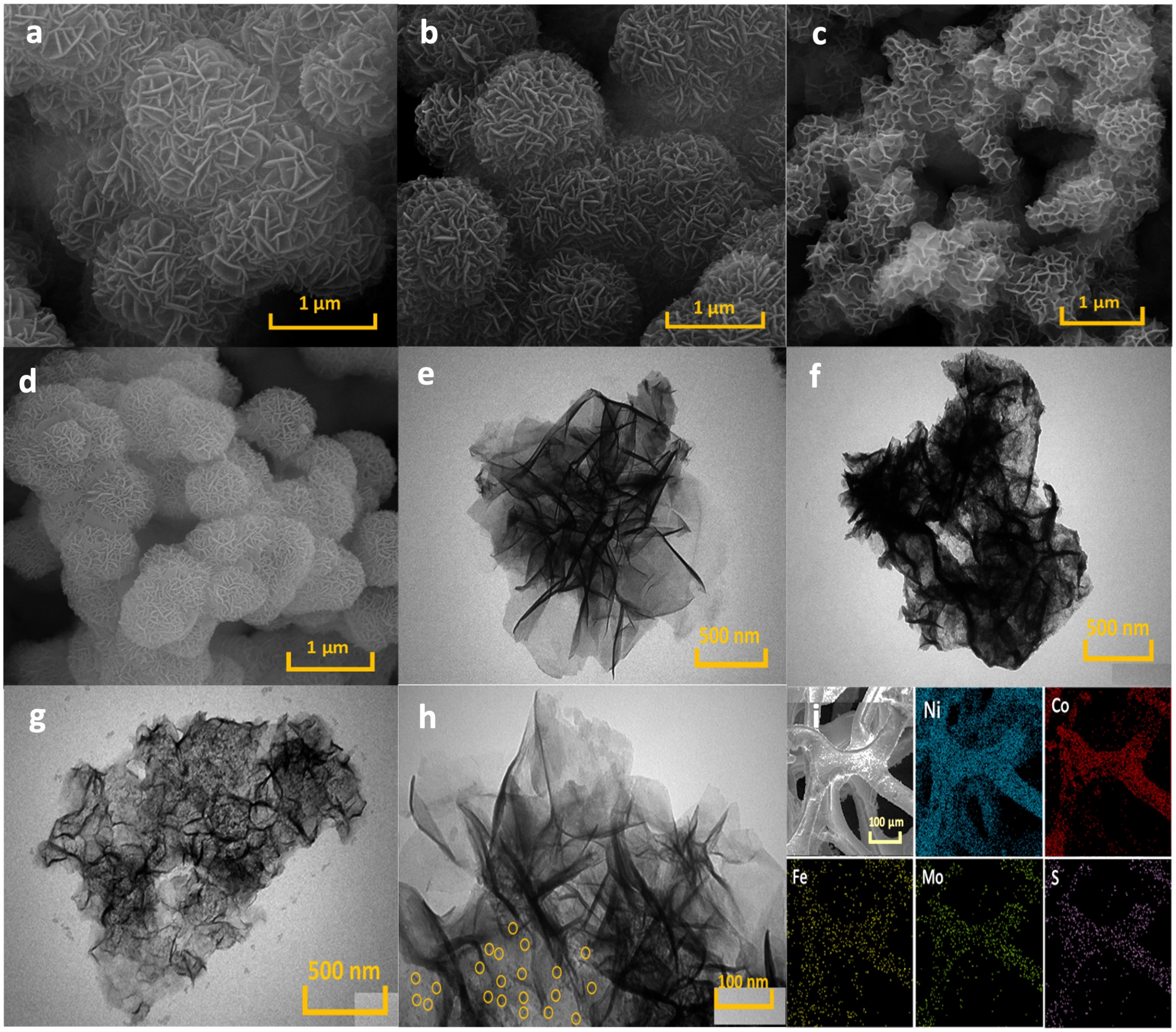

Figure 2: SEM images a) NiFeCo-LDH/NF, b) NiFeCo-Mo(doped)-LDH/NF, c) MoS_2@NiFeCo-LDH/NF, and d) MoS_2@NiFeCo-Mo(doped)-LDH/NF. TEM images e) NiFeCo-LDH, f) NiFeCo-Mo(doped)-LDH, g) MoS_2@NiFeCo-LDH/NF, and h) MoS_2@NiFeCo-Mo(doped)-LDH. Elemental mappings of i) MoS_2@NiFeCo-Mo(doped)-LDH/NF.

XRD analyses were conducted to assess the phases and structures of the LDH materials with and without NF support. Figure 3a reveals distinct peaks at 44.8° and 51.9°, corresponding to the (111) and (200) crystal planes of the NF substrate, respectively.[3,28] Additionally, diffraction peaks at 11.47°, 23.04°, 34.44°, 38.93°, 46.22°, 59.95°, and 61.30°

align with the crystal planes (003), (006), (012), (015), (018), (110), and (113) of the NiFeCo-LDH phase.[65–67] Notably, no distinct diffraction peaks related to Mo doping or MoS_2 QDs can be observed on the NF-supported materials. This is potentially due to their low content compared to the Ni substrate, which suggests that they are present in trace amounts. However, the above SEM-EDS elemental mapping and EDS analyses clearly confirm the presence of Mo and MoS_2 in the LDH samples, we assume that the prominent peaks originating from NF overshadowed the diffraction peaks of Mo and MoS_2 species.

Figure 3b shows that without the NF substrates the introduction of Mo or MoS_2 QDs leads to changes in phases of the Bragg reflections of NiFeCo-LDH. In particular, new phases characterized by modified diffraction patterns and diminished peak intensities can be seen. The XRD analyses of NiFeCo-LDH and NiFeCo-Mo(doped)-LDH without NF substrate reveal that Mo doping reduces the diffraction peaks intensity, increases peak width, and shifts them to a higher angle; together these observations imply that Mo doping decreases the LDH crystallinity and thereby makes the LDHs more amorphous.

X-ray photoelectron spectroscopy (XPS) analysis of MoS_2@NiFeCo-Mo(doped)-LDH, before and after long-term HER, OER and OWS electrocatalysis, was conducted to gain comprehensive understanding on the surface chemical composition and electronic properties of the catalysts. The results in Figures 3 and S5 show the full XPS spectrum of MoS_2@NiFeCo-Mo(doped)-LDH. Figure 3 confirms the presence of Ni, Fe, Co, Mo, S, and O in the catalyst. Furthermore, the high-resolution XPS spectra in Figures 3d, e, f, g, S5 reveal the Ni, Fe, Co, and Mo valence states in MoS_2@NiFeCo-Mo(doped)-LDH. In Figures 3d, 3e, and 3f, the deconvoluted Ni 2p spectrum shows peaks at 852.42 and 855.86 eV, while the Co 2p spectrum has peaks at 776.56 and 780.23 eV. The core-level Fe 2p spectrum exhibits peaks at 707.75 and 719.19 eV, along with two shakeup satellites, indicating the presence of Ni, Fe, and Co in both their elemental and oxidized states (Ni^{2+}, Co^{3+}, and Fe^{3+}, respectively).[9,68–75] After prolonged electrocatalysis, only minor shifts in the positions of the metal 2p peaks towards lower binding energies of the XPS spectra were observed (Figure S5). The small shifts indicate the high durability of the catalyst during the electrocatalysis.

The high-resolution XPS spectrum in Figure 3g shows the Mo 3d and S 2s regions of MoS_2 QDs and the Mo 3d region. The observed peaks at 231.62 eV (Mo $3d_{5/2}$) and 235.6 eV (Mo $3d_{3/2}$) correspond to the Mo^{6+} oxidation state.[47,76] The peaks at 229.01 and 233 eV are indicative of Mo $3d_{5/2}$ and Mo $3d_{3/2}$, respectively, which indicate that the deposited MoS_2 QDs have the 2H phase .[59,74,77] Furthermore, the comparison of high-resolution XPS spectra before and after extended electrocatalysis reveals a minor shift in the Mo peak, which suggests that deposited QDs are highly durable under electrocatalytic conditions. However, the peak position of MoS_2 QDs in the XPS spectrum Mo 3d shifts to 228.54 and 232.12 eV, suggesting the transformation of MoS_2 QDs from the 2H to the 1T' during electrocatalysis.[74] This QD-induced shift has previously been correlated with increased electrical conductivity of the electrode and higher density of electrocatalytic active sites.[74]

The S 2p high-resolution XPS spectrum after electrocatalytic activity reveals distinct peaks at 160.0 and 161.74 eV, corresponding to the S $2p_{3/2}$ and S $2p_{1/2}$ binding energies of S^{2-} in MoS_2 QDs, respectively (Figure 4h).[59,74,77] Noticeably, the S 2p XPS plot peaks position confirms the conversion of the 1T' phase from the 2H phase in MoS_2 QDs after prolonged electrocatalysis.[77] The O 1s XPS spectrum (Figure 2i) can be deconvoluted into three subpeaks at 529.13, 531.69, and 534.26 eV, representing metal-oxygen bonding, defect sites with low oxygen coordination, and adsorbed hydroxy or H_2O, respectively.[3,9,29,78] The O 1s XPS peaks of MoS_2@NiFeCo-Mo(doped)-LDH exhibit a minor shift towards more negative values after a prolonged electrocatalysis, highlighting the high stability of the catalyst (Figure S5). The high-resolution XPS spectrum of MoS_2@NiFeCo-Mo(doped)-LDH following extended electrocatalysis exhibits minor alterations in peak positions for all elements, suggesting high durability of the hierarchical MoS_2@NiFeCo-Mo(doped)-LDH heterostructure.

Overall, the above structural analyses confirm the successful assembly of MoS_2@NiFeCo-Mo(doped)-LDH. These structures feature tight integration of MoS_2 QDs deposited on the NiFeCo-LDH surface and Mo doping in the NiFeCo-LDH matrix.

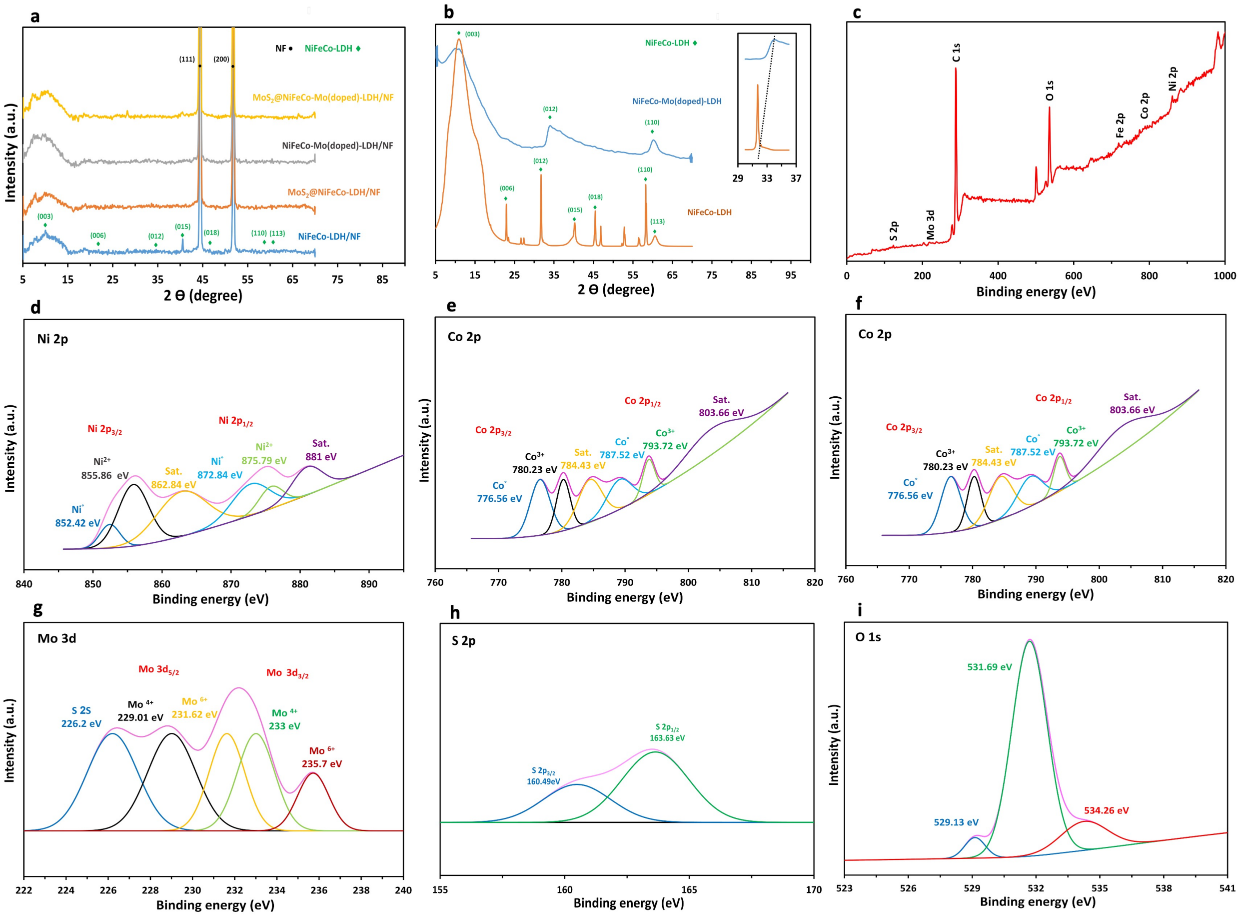

Figure 3: XRD pattern of a) NiFeCo-LDH, MoS_2@NiFeCo-LDH, NiFeCo-Mo(doped)-LDH, and MoS_2@NiFeCo-Mo(doped)-LDH on NF substrate. b) NiFeCo-LDH and NiFeCo-Mo(doped)-LDH without NF substrate. c) Survey XPS spectra of the MoS_2@NiFeCo-Mo(doped)-LDH/NF. XPS spectra d) Ni 2p, e) Co 2p, f) Fe 2p, g) Mo 3d, h) S 2p, and i) O 1s of MoS_2@NiFeCo-Mo(doped)-LDH/NF.

Electrocatalytic performance

The (photo)electrocatalytic performance of the LDH heterostructures towards HER and OER in 1.0 M KOH was assessed using a standard three-electrode cell. Initially, the Ni/Fe/Co ratio was evaluated and optimized to identify the most active NiFeCo-LDHs. The optimization was based on electrocatalytic performance, which was evaluated through linear scanning voltammetry (LSV) at a scan rate of 5 mV s^{-1} (Figure S6), and then by analyzing the corresponding Tafel plots and overpotentials at current densities of 10 and 50 mA·cm^{-2} (Figures S7, and S8) Afterwards, the best-performing electrodes with the high current densities, smallest Tafel slopes, and lowest overpotentials were further functionalized with Mo and MoS_2 to fabricate the NiFeCo-LDH, NiFeCo-Mo(doped)-LDH, MoS_2@NiFeCo-LDH, and MoS_2@NiFeCo-Mo(doped)-LDH electrodes.

The hydrogen evolution reaction

The electrocatalytic performance of NiFeCo-LDH, NiFeCo-Mo(doped)-LDH, MoS_2@NiFeCo-LDH and MoS_2@NiFeCo-Mo(doped)-LDH electrodes towards HER in 1.0M KOH was evaluated under both light illumination and dark conditions. The results were compared with NF and the benchmark Pt/C catalyst. The LSV polarization curves presented in Figure 4a show that at a current density of 10 mA cm^{-2} the overpotentials for Pt/C, NF, NiFeCo-LDH, NiFeCo-Mo(doped)-LDH, MoS_2@NiFeCo-LDH, and MoS_2@NiFeCo-Mo(doped)-LDH as 91, 591, 222, 161, 203, and 104 mV respectively. Under light illumination the overpotential to achieve the 10 mA cm^{-2} current density on MoS_2@NiFeCo-Mo(doped)-LDH and MoS_2@NiFeCo-LDH decreased from 104 to 64 mV and 239 to 203 mV, respectively.

The overpotentials at 10 and 50 mA cm^{-2} HER current densities on the studied materials both under light irradiation and dark conditions are shown in Figure S9 of the Supporting and Table S1, where the HER performance of MoS_2NiFeCo-Mo(doped)-LDH is compared with other recently developed catalysts. The comparison shows that the hierarchical MoS_2NiFeCo-Mo(doped)-LDH heterostructure exhibits very high electrocatalytic HER activity; under dark conditions at 10 mA cm^{-2} the overpotential of MoS_2@NiFeCo-Mo(doped)-LDH is 104 mV, which is only marginally higher than that of the Pt/C benchmark (91 mV) (Figure S9). Under light irradiation, the MoS_2@NiFeCo-Mo(doped)-LDH photoelectrode exhibits an overpotential of 64 mV at a current density of 10 mA cm^{-2}. Overall, the results in Figure S9 clearly show that i) the deposition of MoS_2 QDs increases the (photo)electrocatalytic HER activity more on NiFeCo-Mo(doped)-LDH than on NiFeCo-LDH and ii) Mo doping and MoS_2 significantly improve the electrocatalytic HER activity as compared to the NiFeCo-LDH.

The Tafel analysis in Figure 4b shows that the Tafel slope of MoS_2@NiFeCo-Mo(doped)-LDH is as low as 95 mV dec^{-1}, which is lower than those of NiFeCo-Mo(doped)-LDH (139 mV dec^{-1}), MoS_2@NiFeCo-LDH (175 mV dec^{-1}), and NiFeCo-LDH (161 mV dec^{-1}). Under light illumination the reduces the Tafel slope of MoS_2@NiFeCo-Mo(doped)-LDH further decreases from 95 mV dec^{-1} to 65 mV dec^{-1}. These slopes are rather close to those of commercial Pt/C (49 mV dec^{-1}). The Tafel slopes suggest that the HER likely follows the Volmer–Heyrovsky mechanism[79] with the Heyrovsky step as the rate-determining step (RDS). The spread of the Tafel slopes between different materials is, however, rather significant, which indicates that the HER mechanism may involve different RDSs and that the current density may depend *e.g.* on the mass transfer efficiency.

Electrochemical impedance spectroscopy (EIS) measurements were conducted to provide insights into the charge transfer kinetics during HER. The Nyquist plots depicted in Figure 4c show that the charge transfer resistance (R_{ct}) of MoS_2@NiFeCo-Mo(doped)-LDH (22 Ω cm^{-2}) is smaller than that of the other considered catalysts. Under light illumination, the charge transfer resistance decreases to less than 4 Ω cm^{-2}. These observations imply fast charge transfer kinetics towards HER under both dark and light conditions and clearly illustrate the pivotal role of MoS_2 QDs in expediting charge transfer under light illumination

We measured the double-layer capacitance (C_{dl}) in the non-Faradaic region using cyclic voltammetry (CV) at various scan rates (Figure S10) to provide a semi-quantitative estimate of the electrochemical surface area (ECSA). Figure 4h shows the calculated C_{dl}

values for MoS_2@NiFeCo-Mo(doped)-LDH, MoS_2@NiFeCo-LDH, NiFeCo-Mo(doped)-LDH, and NiFeCo-LDH are 14, 13.4, 12.5, and 7.6 mF cm^{-2}, respectively. This suggests that the incorporation of MoS_2 QDs on and Mo in NiFeCo-LDH leads to a larger ECSA and a higher number of accessible active sites within the hierarchical heterostructure. Remarkably, the deposition of MoS_2 QDs onto NiFeCo-Mo(doped)-LDH and NiFeCo-LDH significantly increases the effective ECSA to 24.3 and 21.5 mF cm^{-2} under light irradiation, respectively. The increase in the effective ECSA indicates that the deposition of ceMoS2 QDs increases the (effective) active surface area or improves the light absorption, both of which are crucial for the (photo)electrocatalytic HER.

The durability of the catalyst under HER conditions was evaluated using chrono-potentiometry (CP) with continuous current measurement at a current density of 10 mA cm^{-2} for over 48 h. As depicted in Figure 4g, the best performing HER electrocatalyst, MoS_2@NiFeCo-Mo(doped)-LDH exhibits a minimal change in the electrode potential, which indicates high stability. This conclusion is supported by the minimal changes in the LSV curves (Figure S11a) recorded before and after 500-cycle voltammetry scans under dark conditions. MoS_2@NiFeCo-Mo(doped)-LDH maintains its high stability and (photo)electrocatalytic activity even after is subjected to an additional 500 CV cycles under light illumination, as shown in Figure S11b. This is rather surprising, as we initially assumed that the amorphization due to Mo doping would reduce the catalyst stability; in contrary to our expectations, MoS_2@NiFeCo-Mo(doped)-LDH exhibited exceptional stability under (photo)electrocatalytic HER conditions. Currently, we do not understand the origin of the increased durability but it is clear that some complex synergistic effects between doped Mo, MoS_2 QDs, and NiFeCo-LDH result in a very stable (photo)electrocatalytic material.

Overall, our results indicate that introducing Mo and MoS_2 QDs makes the NiFeCo-LDH a highly active and stable HER (photo) electrocatalyst under alkaline conditions. The high activity is tentatively attributed to both geometric and electronic modifications resulting from the introduction of Mo in and MoS_2 on the FeNiCo-LDH, which is also supported by the computational results below.

The oxygen evolution reaction

The OER performance of the LDH electrocatalysts was evaluated in 1 M KOH solution under light irradiation and dark conditions, and compared to the benchmark catalyst RuO_2. As depicted in Figure 4d, the hierarchical MoS_2@NiFeCo-LDH nanostructure exhibits the best and remarkably high OER activity: as shown in Figure S9 and Table S2, the OER overpotential of MoS_2@NiFeCo-LDH at 10 mA cm^{-2} is only 217 mV and is even lower than that of most the prior studies and benchmark RuO_2, which has an overpotential of 327 mV at 10 mA cm^{-2}. Under light illumination, the overpotential of MoS_2@NiFeCo-LDH is further reduced from 217 mV to 178 mV at a current density of 10 mA cm^{-2}. For the other LDH catalysts, the impact of light illumination is smaller and on *e.g.* MoS_2@NiFeCo-Mo(doped)-LDH the overpotential reduces from 227 mV to 225 mV at a current density of 10 mA cm^{-2}. The results in Figures 4d and 4e clearly show the MoS_2 QDs can significantly enhance the OER photoelectrocatalytic activity of the different LDHs but the effect varies on the underlying LDH matrix. Among the studied LDHs, MoS_2@NiFeCo exhibits the best photo- electrocatalytic activity towards OER. Interestingly, the Mo-doping seems to make the materials less active towards OER whereas the opposite was observed for HER. Moreover, the LSV curves depicted in Figure S12 indicate that doping of Mo does not affect the activity of NiFeCo-LDH under light irradiation, highlighting the role of doping high-valence metals or creating defects and deposition of MoS_2 QDs in the (photo)electrocatalytic OER.

Besides the low overpotential observed for MoS_2@NiFeCo-LDH, this material has a low Tafel of slope 73 mV dec^{-1} as shown in Figure 4e. The concomitant Mo-doping and MoS_2 incorporation lead to an even lower Tafel slope. The MoS_2NiFeCo-Mo(doped)-LDH exhibits a very low slope of 57 mV dec^{-1}, which is lower than observed for MoS_2@NiFeCo-LDH and NiFeCo-Mo(doped)-LDH (126 mV dec^{-1}). Both MoS_2@NiFeCo-LDH and MoS_2NiFeCo-Mo(doped)-LDH have lower Tafel slopes than the commercial RuO_2 catalyst (94 mV dec^{-1})

but Tafel slope of NiFeCo-LDH (39 mV dec^{-1}) is even smaller. The Tafel slope analysis also indicates that the incorporation of MoS_2 QDs and Mo doping changes the RDS;[79] we ascribe the decreases in the Tafel slopes from ∼60 to ∼40 mV dec^{-1} to a change in the RDS from a chemical transformation after the first electron transfer to the second electron transfer step, that is from *O to *OOH formation (Equation 3 and 4).[79] Under light irradiation, an extremely slow Tafel slope is observed for both MoS_2@NiFeCo-LDH (32 mV dec^{-1}) and MoS_2@NiFeCo-Mo(doped)-LDH (38 mV dec^{-1}). Altogether, the alkaline OER activity of MoS_2@NiFeCo-LDH, under both light irradiation and dark conditions, surpasses that of most state-of-the-art OER catalysts, as shown in Table S2 of the Supplementary Information.

The EIS analysis and Nyquist plots in Figure 4f illustrate the impact of QDs on charge transfer resistance in the OER process. MoS_2@NiFeCo-LDH has the lowest resistance (8.5 Ω cm^{-2}) in the low-frequency regime. The resistance further decreases below 4 Ω cm^{-2} upon light irradiation. These observations suggest that MoS_2@NiFeCo-LDH has very low charge transfer resistance and fast OER kinetics. Furthermore, the photogenerated charge carriers (electrons and holes) contribute to enhanced conductivity under light illumination and accelerate electrochemical reactions.

Similarly to HER, the MoS_2@NiFeCo-LDH catalyst demonstrates notable durability in alkaline media at a current density of 10 mA cm^{-2}. Indeed, the data in Figure 4g shows that MoS_2@NiFeCo-LDH remains very stable for over 48 h under OER conditions. Moreover, the LSV curves before and after 500 cycles in Figure S11c provide evidence of MoS_2@NiFeCo-LDH's excellent durability under OER conditions. The stability is not affected by additional, 500 cycles under light illumination, as shown in Figure S11d.

Overall, our results show that depositing MoS_2 QDs on NiFeCo-LDH results in a very stable and active OER (photo)electrocatalyst. The EIS results show that the MoS_2 QDs reduce the transfer resistance, which indicates that the QDs enhance the OER kinetics. The addition of MoS_2 QDs also reduces the Tafel slope and changes the RDS from *O to *OOH formation.

Overall Water Splitting

Inspired by the exceptional performance of MoS_2@NiFeCo-LDH towards OER and MoS_2@NiFeCo-Mo(doped)-LDH toward HER, these materials were used as the anode and cathode, respectively, in a two-electrode water electrolysis cell. Figure 4i shows the polarization curves in 1.0 M KOH solution for the assembled MoS_2@NiFeCo-Mo(doped)-LDH‖MoS_2@NiFeCo-LDH electrolyzer under both light irradiation and dark conditions, along with the comparison with Pt/C‖RuO_2 as the benchmark cell. The results show that the MoS_2@NiFeCo-Mo(doped)-LDH‖MoS_2@NiFeCo-LDH cell requires 1.54 V (1.85 V) voltage to achieve the current densities of 10mA cm^{-2} (100 mA $cm^{-2)}$ (see also Video S1 (under dark), S2 (under light)). Under light irradiation, the voltage decreases to 1.46 V and 1.68 V at current densities of 10 and 100 mA cm^{-2}, respectively. This performance surpasses the performance of Pt/C‖RuO_2 and most reported OWS electrolyzers, as shown in Table S3.

The MoS_2@NiFeCo-Mo(doped)-LDH‖MoS_2@NiFeCo-LDH cell also demonstrates remarkable stability for at least 48 h as shown in Figure 4g. There are no significant changes from the initial potential at a constant current density of 10 mA cm^{-2}, reflecting high stability of the overall cell and both electrodes. Even after prolonged electrocatalysis only negligible changes in the structures and the ratio of elements at the surface were observed through SEM and XPS(Figures S5 and S13). This high overall water splitting performance positions MoS_2@NiFeCo-Mo(doped)-LDH and MoS_2@NiFeCo-LDH as one of the best Ni-, Fe-, and Co-based electrocatalysts for HER, OER and OWS developed recently (see Tables S1, S2, and S3).

Correlating (Photo)Electrocatalytic Performance with Structural and Morphological Features

The SEM and TEM analyses in Figures 2b and S1 clearly illustrate that Mo doping in NiFeCo-LDH results in the formation of thicker and denser nanosheets. While decreasing the LDH nanosheet thickness has been observed to improve the charge conductivity and to increase the electrocatalytic activity,[3,28,80,81] our findings show that doping the NiFeCo-LDH by Mo leads to both thicker sheets and increased HER activity. This discrepancy between our and previous results can be explained by the XRD results shown in Figure 3b, which shows that Mo doping causes the amorphization of the crystalline NiFeCo-LDH structures. Most notably, the higher degree of amorphization has been correlated with enhanced electrocatalytic activity due to the increased number of active sites and structural flexibility.[25,26,28,29]

On the other hand, the deposition of MoS_2 QDs reduces the overall thickness of the LDH sheets and improves the HER and OER activity. Correlating the TEM and SEM analysis with electrocatalytic studies indicates the enhanced electrocatalytic activity following MoS_2 deposition is not due to increased amorphization. Instead, the ECSA analysis shows that the MoS_2 increases the number of active sites. The combination of Mo doping and MoS_2 QDs deposition both increases amorphization, decreases the sheet thickness and increases the ECSA. It appears that the increased amorphization and thickness are both beneficial for enhancing the (photo)electrocatalytic HER activity while for OER benefits only from the increased ECSA.

The XPS analysis in Figure 3 and S5 show the peak positions of MoS_2@NiFeCo-Mo(doped)-LDH are not altered when used as a (photo)electrocatalyst for a prolonged time. However, the surface composition of the components does exhibit some variation compared to the initial state in MoS_2@NiFeCo-Mo(doped)-LDH following extended electrocatalysis (Figure S5). Figure S11 also shows that both the HER and OER electrocatalytic performance remains rather unaffected by 500 CV cycles. Under photoelectrocatalytic conditions, the performance of MoS_2@NiFeCo-Mo(doped)-LDH is slightly decreased but we were not able to correlate this change in any structural or morphological changes. Altogether, the changes in the composition, structure, morphology, and (photo)electrocatalytic activity of MoS_2@NiFeCo-Mo(doped)-LDH are modest, which underscores the high stability of the catalysts under electrocatalytic conditions.

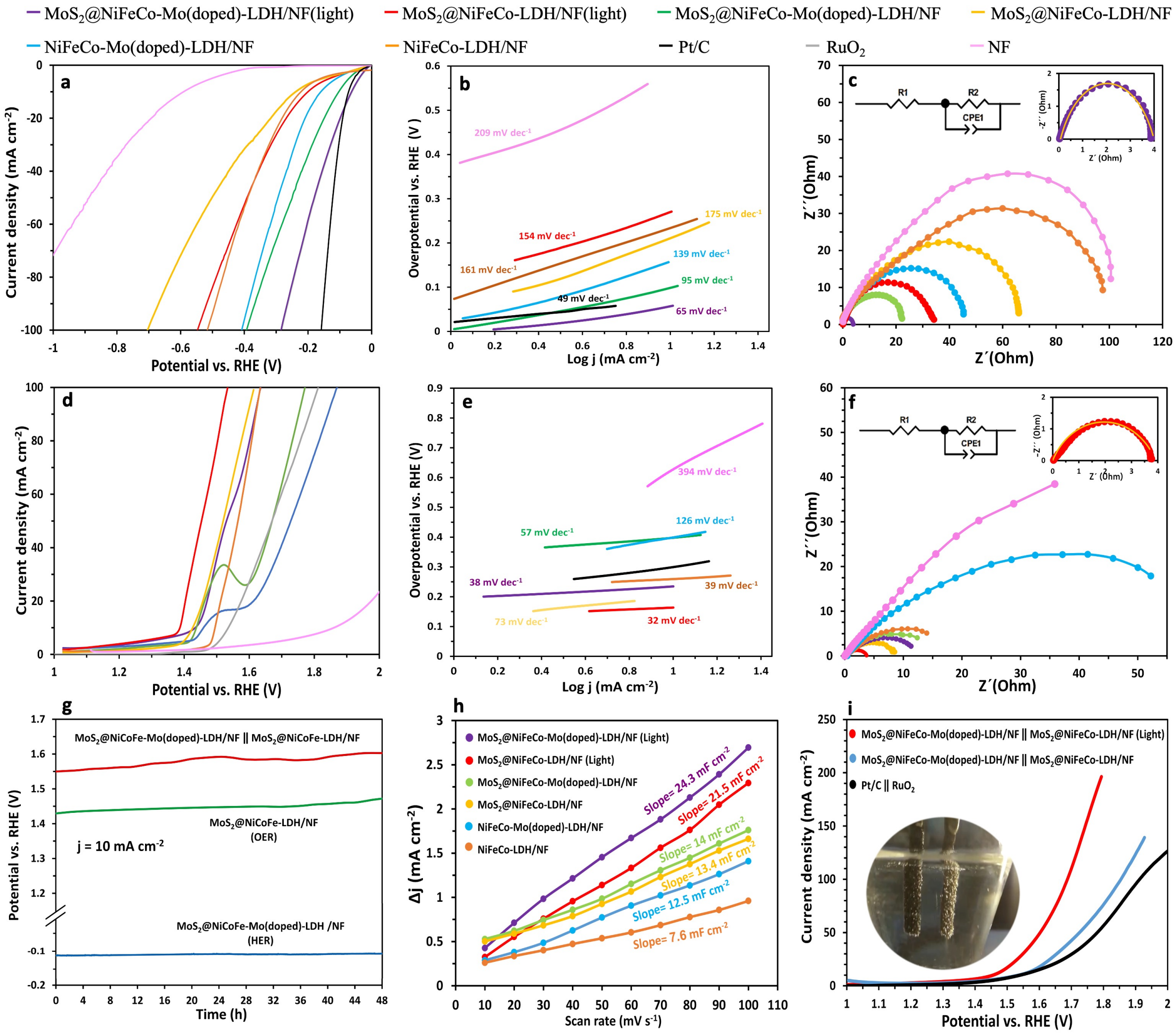

Figure 4: HER and OER electrocatalytic performance of the as-prepared catalysts under light irradiation and dark conditions. a) HER polarization curves. b) Tafel slope of the as-synthesized electrocatalysts for HER. c) Electrochemical impedance spectroscopy for HER. (The inset provides a magnified representation of the MoS_2@NiFeCo-Mo(doped)-LDH catalyst under light irradiation.) d) OER polarization curves. e) Tafel slope of the as-synthesized electrocatalysts for OER. f) Electrochemical impedance spectroscopy for OER. (The inset provides a magnified representation of the MoS_2@NiFeCo-LDH catalyst under light irradiation.) g) Long-term stability test of MoS_2@NiFeCo-Mo(doped)-LDH, MoS_2@NiFeCo-LDH, and MoS_2@NiFeCo-Mo(doped)-LDH‖MoS_2@NiFeCo-LDH electrolyzer for HER, OER, OWS, respectively. h) Double-layer capacitance of as-synthesized electrocatalysts. i) Polarization curves of the MoS_2@NiFeCo-Mo(doped)-LDH‖MoS_2@NiFeCo-LDH heterostructure under light irradiation and dark conditions in a two-electrode system, compared to Pt/C‖RuO_2.

Computational studies of OER and HER

Density functional theory (DFT) calculations were carried out to understand how and why MoS_2 QDs and Mo doping impact the HER and OER activity of NiFeCo-LDH. To achieve this, we studied how the HER/OER thermodynamics depend on the Ni/Fe/Co ratio, nature of the active site, Mo doping, and MoS_2-QD deposition using the structures shown in Figure S14. The activity was quantified by computing the reaction thermodynamics under alkaline reaction conditions using the computational hydrogen electrode method[82] and by studying the electronic structure properties.

The DOS plots for NiFeCo-LDHs with varying metal ratios, and in the presence of Mo dopants and MoS_2 QDs, are presented in Figures 5a and S15. The semiconducting nature of $Ni_4Fe_1Co_3$, $Ni_7Fe_4Co_1$, and $Ni_7Fe_2Co_1$ LDHs is evident in Figure S15. These results also show that by adjusting the metal ratio, one can influence the band gap and the electronic structure, and thereby also the electrocatalytic performance of LDHs. Doping Fe/Ni/Co-LDH with Mo or by incorporating MoS_2 QDs on the LDH leads to the disappearance of the band gap and makes the semiconducting LDH catalysts metallic, which could increase the electrode conductivity. Furthermore, the charge transfer between MoS_2 QDs and NiFeCo-LDH or NiFeCo-Mo(doped)-LDH can be seen by analyzing the Bader charges (Figure S16), which reveal a significant electron transfer from NiFeCo-LDH or NiFeCo-Mo(doped)-LDH to the MoS_2 QDs. Interestingly, the Mo doping of NiFeCo-LDH results in a slightly increased electron transfer from LDH to the MoS_2 QDs.

The hydrogen absorption energy (ΔG_{H^*}) is a widely used descriptor for the HER performance of a catalyst. The optimal ΔG_{H^*} value has traditionally been taken as 0 eV but more recent studies have shown that the optimal binding energy is slightly endothermic, $\sim$ 0.1-0.2 eV, at zero overpotential.[83] The free energies of the adsorbed H at different sites on the top and edge sides of heterostructures are depicted in Figures 5b and S17-22. Variations in the Fe, Ni, and Co ratios notably influence the hydrogen adsorption energy, as illustrated in Figures S17-19. This indicates that control over the metal ratio efficiently tunes the LDH activity towards HER. Specifically, $Ni_7Fe_2Co_1$ LDH has near optimal hydrogen binding energies at different sites whereas the other LDH compositions do not. This indicates that $Ni_7Fe_2Co_1$ is a near ideal and active HER catalysts; this is consistent with our experimental findings in the previous sections.

As shown in Figures 5a and S20-22, doping, modifying the $Ni_7Fe_2Co_1$ LDH by Mo doping and/or MoS_2 QDs have a significant impact on the hydrogen adsorption energy. Our results show that the top site and Fe sites bind hydrogen weakly and are expected to be catalytic inactive towards HER, while the other sites have near optimal hydrogen binding. In particular, the MoS_2@$Ni_6Fe_2Co_1$-Mo(doped) heterostructure catalyst has a near optimal hydrogen binding energy of 0.32 eV on Co sites. Contrasting these computational results with the electrocatalytic activity tests in Figure 4 a-c shows that the hydrogen binding energies can be used as a reliable descriptor for the HER activity: the incorporation of Mo and MoS_2-QDs in the Fe/Ni/Co LDHs leads to near optimal hydrogen energies, which correlate with the experimentally observed lower overpotentials, smaller Tafel slopes, and smaller charge transfer resistances. The computational results show that both Mo and MoS_2-QDs significantly enhance the HER activity of the Fe/Ni/Co-catalysts.

The alkaline OER generally involves four proton-electron transfer steps and three main intermediates, OH^*, O^* and OOH^*, as shown in Figure 5c. We assume that the OER follows the adsorbate evolution mechanism (AEM) identified as the most likely mechanism on NiFe-LDHs under electrode potential conditions relevant for OER.[84] In this work, we quantify the OER performance using the concept of thermodynamic overpotential, which measures the electrode potential needed for making all the steps thermodynamically feasible as discussed in the methods section. Within this thermodynamic framework, the OER efficiency is determined by the elementary step having the most endergonic reaction energy, which is assigned as the potential-determining step (PDS). We carried out this analysis for a range of experimentally studied catalysts with varying metal ratios and at different active sites.

The results in Figures 5d and S23-28 show the main computational results for the various LDH heterostructure catalysts towards OER. Figure 5d shows that the Fe and Co sites of the $Ni_7Fe_2Co_1$ electrode have lowest thermodynamic OER overpotentials among the MoS_2-NiFeCo-LDHs, which in the experiments exhibited the were it was shown that the best OER performance among the studied catalysts. Additionally, the formation of *O from *OH was identified as the PDS for all sites in the $Ni_7Fe_2Co_1$ LDH (Figure S25). However, the comparison of Figures 5d and S23-27 shows that MoS_2@NiFeCo does not have the lowest thermodynamic overpotential among the studied structures; instead, the NiFeCo-LDH (Figure S25) structure is found to exhibit significantly lower thermodynamic overpotentials. This computational finding is, however, not consistent with the experimental results in Figures 4d and 4e, which show that MoS_2@NiFeCo is a better OER catalyst than NiFeCo.

To resolve the discrepancy between the experimental and computational results on the OER activity, we need to consider which elementary steps determine the PDS. Without MoS_2 incorporation and Mo doping, *i.e.* on $Ni_4Fe_1Co_3$, $Ni_7Fe_4Co_1$, and $Ni_7Fe_2Co_1$), the formation of O^* from OH^* is the PDS. This would indicate that the strong O^* adsorption limits the OER efficiency on these catalysts without Mo or MoS_2. Furthermore, the computed overpotential trend observed for Ni/Fe/Co LDHs align with those obtained in our experiments for LDHs with various metal ratios, as illustrated in Figure S8. Interestingly, the QD addition and Mo doping change the PDS from O^* formation to OOH^* formation on the Fe and Ni sites (Figures 5d and S26-28); this change in the rate-determining step is also supported by the experimental Tafel slope analysis for OER as discussed above. We attribute this change in the PDS to the electronic interaction between LDH and MoS_2 QDs which enhances OER activity by reducing the ΔG on of the OOH^* formation step. For instance, the introduction of MoS_2 on $Ni_7Fe_2Co_1$ does not notable impact though the formation energy of *O but the formation energy *OOH is facilitated at the Fe site, which changes the PDS from *O to *OOH (Figure 5d).

In addition to changing the PDS from O^* to OOH^*, MoS_2 is also expected to change reaction kinetics. In particular, the constant potential DFT studies in Ref. 84 indicate that the OOH^* generation is the slowest and hence the rate-determining step of OER following the AEM mechanism on NiFe-LDHs. This indicates that even if O^* formation would determine the thermodynamic overpotential and be the PDS, the OOH^* formation would be the RDS and determine the overall activity. Taking this into account and using the free energy relations between reaction thermodynamics and kinetics, we are led to the conclusion that facilitating the OOH^* formation would also result in the largest increase in the reaction kinetics and thereby OER efficiency. This in turn indicates that the introduction of MoS_2 QDs onto LDH structures would lead to the most pronounced enhancements in the OER efficiency because MoS_2 QDs most significantly facilitate OOH^* formation thermodynamics. Hence, if we account for the observation that OOH^* formation determines the OER kinetics and facilitating the thermodynamics of this step leads to the largest enhancements in the OER efficiency, our computational results are in line with our experimental results showing that the incorporation of MoS_2 QDs leads to very efficient OER.

Overall, our computational results show that control over the metal ratio, Mo doping, and MoS_2 incorporation are efficient ways of controlling the electronic structure and electrocatalytic properties of LDH heterostructures. The electronic structure analysis shows that doping Mo into and the deposition of MoS_2 QDs onto NiFeCo-LDH make the catalyst metallic, which likely increases conductivity. The MoS_2 deposition also leads to significant electron transfer from the LDH to the QD and likely promotes electrocatalytic activity near the QD. We also find that the thermodynamic overpotentials can explain the experimentally observed HER activity across the studied materials; this indicates that the HER activity of LDH heterostructures can be understood based on reaction thermodynamics and explains why the MoS_2-NiFeCo-Mo(doped)-LDH is such an active HER electrocatalyst. The OER is significantly more complex and the experimental results cannot be understood without accounting for reaction kinetics in addition to the thermodynamics. However, even for OER, the thermodynamic analysis helps to identify how different modifications change the reaction mechanism and thermodynamics. In particular, when one considers that OOH^* formation determines *both the thermodynamics and kinetics*, it appears that one can explain the high OER activity of MoS_2-NiFeCo-LDH by considering the thermodynamics of the RDS only. However, it needs to be stressed that the experimentally measured overpotential is kinetic in nature, which means that accounting for reaction kinetics, incorporating solvent, cation, and electrode potential effects, and coupling of DFT and microkinetic modeling are needed to make reliable and self-consistent predictions on the OER activity.[85]

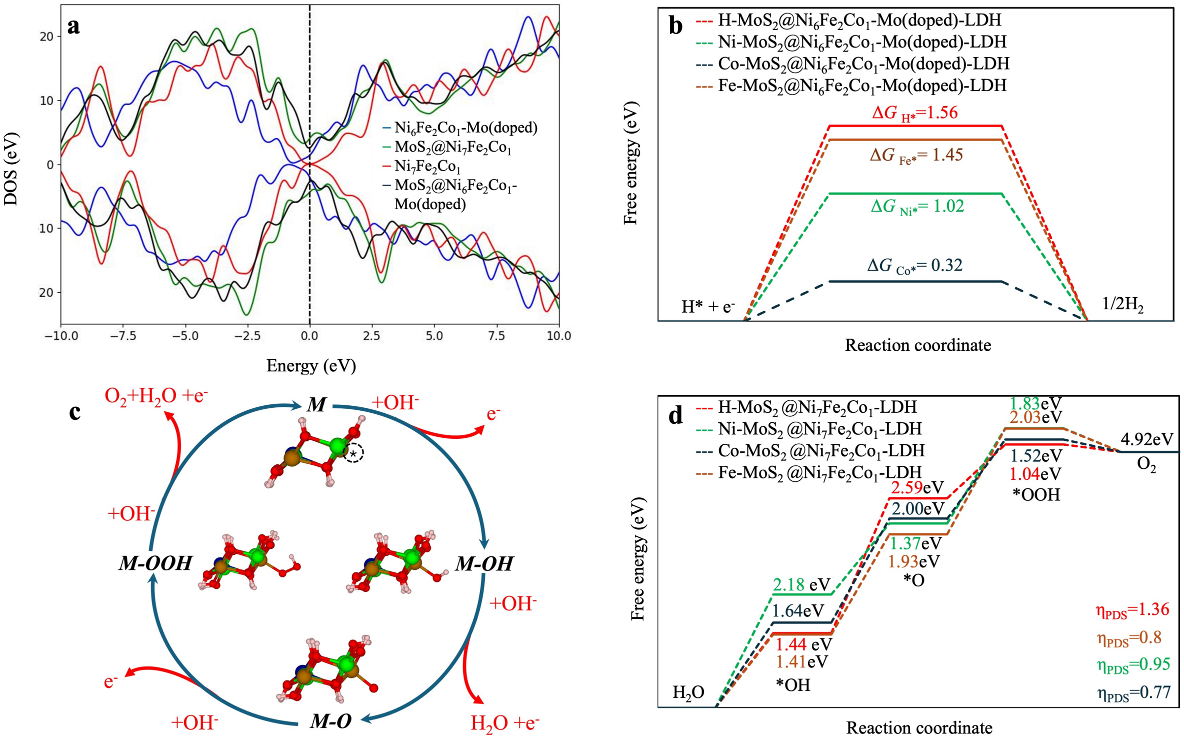

Figure 5: a) DOS profiles of NiFeCo-LDH, NiFeCo-Mo(doped)-LDH, MoS_2@NiFeCo-LDH, and MoS_2@NiFeCo-Mo(doped)-LDH. b) Gibbs free energy diagram of MoS_2@NiFeCo-Mo(doped)-LDH for HER process on hollow, Ni, Fe, and Co sites. c) Schematic diagram of the OER mechanism. d) Gibbs free energy diagram of MoS_2@NiFeCo-LDH for OER process on hollow, Ni, Fe, and Co sites.

Conclusions

In this work, we have developed a facile and modular multistep procedure to synthesise hierarchical LDH-based heterostructure electrocatalysts, MoS_2@NiFeCo-Mo(doped)-LDH. This synthesis involves the hydrothermal growth of trimetallic nanoflower-like NiFeCo-LDH onto a nickel foam substrate, subsequent high-valence metal Mo doping into NiFeCo-LDH, and final electrodeposition of MoS_2 QDs on the LDH. The efficient and controllable approach for functionalizing NiFeCo-LDHs with MoS_2 quantum dots and Mo dopants allowed for a systematic study on the MoS_2@NiFeCo-Mo(doped)-LDHs. We find that the best MoS_2@NiFeCo-Mo(doped)-LDH and MoS_2@NiFeCo-LDH heterostructures exhibited very high activity towards HER and OER under both light irradiation and dark conditions in alkaline media.

MoS_2@NiFeCo-LDH and MoS_2@NiFeCo-Mo(doped)-LDH were found to have very low OER and HER overpotentials of 178 (217) mV and 64 (104) mV at 10 mA cm^{-2} under light irradiation (dark condition), respectively. In comparison to NiFeCo-NF, the MoS_2@NiFeCo-Mo(doped)-LDH and MoS_2@NiFeCo-LDH heterostructures demonstrated significantly enhanced reaction kinetics and improved light absorption efficiency; these experimental findings are tentatively attributed to the large atomic radius of the high-valence Mo dopant and the photo-responsive nature of MoS_2 QDs, which together change the (photo)electrodes intrinsic HER and OER activity, lead to catalyst amorphization, and increase the effective catalytic surface area. Our DFT studies show that the incorporation of MoS_2 increases the intrinsic electrocatalytic activity of NiFeCo-LDH and NiFeCo-Mo(doped)-LDH towards HER and OER, respectively. The increased activities are due to changes in the electronic structure, reaction thermodynamics, and the reaction mechanism. MoS_2 makes the catalysts metallic and hence enhances their conductivity. MoS_2 QD deposition reduces the free energy barriers of both HER; the incorporation of MoS_2 QDs leads to a nearly ideal energy *H adsorption energy. In OER, MoS_2 changes and facilitates the rate-determining step of OOH* formation at smaller overpotentials; this is also supported by the experimental results. Finally, theMoS_2@NiFeCo-Mo(doped)-LDH and MoS_2@NiFeCo-LDH electrodes exhibit remarkable activity and stability for the overall water splitting efficiency, resulting in potentials of 1.46 (1.54) V at 10 mA cm^{-2}, under light illumination (dark) conditions

Overall, our work provides a facile, modular, and rational approach to design and synthesize hierarchical LDH heterostructures with high (photo)electrocatalytic performance towards OER, HER, and overall water splitting.

Experimental and Computational Methods

Materials

Cobalt(II) chloride hexahydrate ($CoCl_2 \cdot 6\,H_2O$), Iron(III) chloride hexahydrate ($FeCl_3 \cdot 6\,H_2O$), Nickel(II) chloride hexahydrate ($NiCl_2 \cdot 6\,H_2O$), trisodium citrate dihydrate ($C_6H_9Na_3O_9$), urea (CH_4N_2O), ammonium molybdate tetrahydrate ($(NH_4)6\,Mo_7O_{24} \cdot 4\,H_2O$), potassium hydroxide (KOH), potassium chloride (KCl), ammonium tetrathiomolybdate ($(NH_4)2\,MoS_4$), platinum carbon (Pt/C), and ruthenium oxide (RuO_2) were purchased from Merck. The reagents were utilized without additional purification steps. Deionized water (DW) was employed throughout the experimental procedures.

Synthesis of NiFeCo-LDH/NF and NiFeCo-Mo(doped)-LDH/NF

To prepare the NiCoFe-LDH catalysts supported on nickel foam (NF), a 2 × 2 cm^2 piece of NF was first subjected to ultrasonic pretreatment using ethanol and water. Next, the NF was washed in 6.0 M HCl solution and dried at 60 °C. After this, a uniform solution of $CoCl_2 \cdot 6\,H_2O$ (0.4 mmol), $NiCl_2 \cdot 6\,H_2O$ (2.4 mmol), $FeCl_3 \cdot 6\,H_2O$ (0.8 mmol), $C_6H_9Na_3O_9$ (0.5 mmol) and urea (8.0 mmol) dissolved into 30 mL of DW was prepared. The solution was vigorously stirred for 15 minutes and purged with nitrogen (N_2) for 5 minutes. The pretreated NF was then immersed in this solution, and the entire mixture was transferred to a 50 mL Teflon-lined stainless-steel autoclave, heated to 150 °C, and maintained for 48 hours. The resultant product was gathered and rinsed multiple times with DW and ethanol, and dried at 80 °C under vacuum.

For the preparation of NiCoFe-Mo(doped)-LDH/NF, 0.02 mmol of $(NH_4)6\,Mo_7O_{24}{\cdot}4\,H_2O$ was dissolved in 30 mL of DW through vigorous stirring until complete dissolution. Then, $CoCl_2{\cdot}6\,H_2O$ (0.4 mmol), $NiCl_2{\cdot}6\,H_2O$ (2.4 mmol), $FeCl_3{\cdot}6\,H_2O$ (0.8 mmol), $C_6H_9Na_3O_9$ (0.5 mmol) and urea (8.0 mmol) were dissolved in the solution, stirred vigorously for 15 minutes and purged with N_2 for 5 minutes. Subsequently, NF was immersed in the solution, transferred to a 50 mL Teflon-lined stainless-steel autoclave, and subjected to heating at 150 °C for 48 hours. The resultant product underwent multiple rinses with DW and ethanol, followed by drying at 80 °C under vacuum.

Synthesis of MoS_2@NiFeCo-LDH/NF and MoS_2@NiFeCo-Mo(doped)-LDH/NF

The electrosynthesis of MoS_2NiFeCo-LDH and MoS_2NiFeCo-Mo(doped)-LDH was conducted using a similar procedure for both electrodes in a three-electrode cell setup under ambient temperature conditions, employing NiFeCo-LDH/NF and NiFeCo-Mo(doped)-LDH/NF (2 × 2 cm^2) as the working electrodes, a platinum plate as the counter electrode, and an Ag/AgCl reference electrode. MoS_2-QDs were electrodeposited on NiFeCo-LDH and NiFeCo-Mo(doped)-LDH in an electrodeposition electrolyte containing 0.5 mmol $(NH_4)2\,MoS_4$ and 0.1 mol KCl. Electrodeposition was carried out in the electrolyte under an applied bias voltage of -0.96 V. The resulting samples were washed using DW and then dried at 60 °C for 3 hours.

Electrochemical measurements

The (photo)electrochemical catalyst tests were conducted at room temperature using a conventional three-electrode system. The catalyst (2 × 2 cm^2), fabricated on an NF substrate, was utilized as the working electrode, a platinum wire served as the counter electrode, and

Ag/AgCl (3M KCl) was employed as the reference electrode. OER and HER tests were conducted in a 1 M KOH electrolyte using the Metrohm potentiostat/galvanostat (Type 1.757.0010) electrochemical workstation. An LED lamp with an optical power of 9 W was used as the illumination source in the photoelectrochemical experiments.

The linear-sweep voltammetric (LSV) polarization curves were measured to evaluate the electrocatalytic performance of the materials. A scan rate of 5 mV s^{-1} was employed in all LSV experiments. The applied potentials are reported on the reversible hydrogen electrode (RHE) scale obtained by using the equation $E_{\mathrm{RHE}} = E_{\mathrm{Ag/AgCl}} + 0.059\mathrm{pH} + E^{0}{}_{\mathrm{Ag/AgCl}}$, where E_{RHE} represents the potential of RHE. The reference electrode, Ag/AgCl, has a standard electrode potential ($E_{\mathrm{Ag/AgCl}}$) of 0.197 V and the overpotential (η) can be determined using $\eta = E_{\mathrm{vs.RHE}} - E_{\mathrm{theoretical}}$, where the theoretical potentials for OER and HER relative to RHE are 1.23 V and 0 V, respectively. The Tafel slope (b) were calculated using the equation $\eta = a + b \log_{10} j$, where η denotes the overpotential, b the Tafel slope, and j the current density.

Cyclic voltammetry (CV) measurements were carried at various scan rates ranging from 10 to 100 mV s^{-1} within the (non-Faradaic) potential window of -0.02 – 0.03 V vs Ag/AgCl. The electrochemical surface area (ECSA) was estimated by evaluating the double-layer capacitance (C_{dl}) values using the equation $C_{\mathrm{dl}} = I/\nu$, where I represents the current density (mA cm^{-2}), and ν is the scan rate (mV s^{-1}). Electrochemical impedance spectroscopy (EIS) measurements were performed using a standard three-electrode system, employing a ZAHNER electrochemical workstation (model IM6ex, Germany). The frequency range of the investigation spanned from 0.1 Hz to 10 kHz, with an applied amplitude of 5 mV. The OWS process was conducted using a two-electrode cell setup, where the MoS_2@NiFeCo-LDH and MoS_2@NiFeCo-Mo(doped)-LDH catalysts served as the anode and the cathode electrodes, respectively.

DFT calculations

The OER and HER mechanisms and free energies on the experimentally studied LDH-based catalysts were studied using spin-polarized density functional theory (DFT) calculations were performed as implemented in the GPAW code[86] within the projector augmented wave (PAW)[87] method. The exchange-correlation effects were treated within the Generalized Gradient Approximation (GGA) and the Hubbard $+U$ correction by employing the Hubbard-corrected Perdew-Burke-Ernzerhof (PBE+U) functional.[88] The Hubbard U corrections were applied to account for strong d-electron correlation with U values 4 eV for the Ni atom, 5 eV for the Fe atom, and 3.2 eV for the Co atom.[89] The U corrections was not employed for Mo due to its broad d bands.

The simulation model, depicted in Figure S14, is based on prior research[90] showing that the layer-layer interactions have no significant impact on the electronic structure and that a single layer of LDH is a reliable model for the LDH catalysts. We simulated the LDH with full OH coverage to resemble the alkaline OER reaction conditions.[90] Further details regarding the cell parameters are provided in the Supporting Information (Table S4). The first Brillouin zone of the supercell was sampled using a 3 × 2 × 1 k point mesh for the top side model and a 3 × 1 × 2 k point mesh for the edge side model. The electronic structure convergence criteria was set to 10^{-5} eV. Atomic forces were converged below 0.1 eV/Å. The plane wave cutoff was set to 450 eV. A vacuum region of 15 Å along the non-periodic direction was included to prevent interactions between the periodic images.

The Gibbs free energy of intermediates involved in HER and OER processes, denoted as *H, *OH, *O, and *OOH, as a function of the electrode potential were computed using the computational hydrogen electrode method:[82]

$$\Delta G = \Delta E_{\mathrm{ads}} + \Delta E_{\mathrm{ZPE}} - T\Delta S - eU_{\mathrm{RHE}} \tag{1}$$

Here, ΔE_{ads} represents the adsorption energy of the intermediate, ΔE_{ZPE} is the change in the zero-point energy, ΔS is the entropy change, T is the temperature (298.15 K), and eU_{RHE} is the applied electrode potential on the RHE scale.

In the alkaline media, OER can proceed *via* through several reaction mechanisms.[91] Here we assume that the OER follows the adsorbate evolution mechanism (AEM) identified as the most likely mechanism on NiFe-LDHs.[84]

OER mechanism:

$$* + \mathrm{OH}^- \rightarrow \mathrm{OH}^* + \mathrm{e}^- \tag{2}$$

$$\mathrm{OH}^* + \mathrm{OH}^- \rightarrow \mathrm{O}^* + \mathrm{H_2O(l)} + \mathrm{e}^- \tag{3}$$

$$\mathrm{O}^* + \mathrm{OH}^- \rightarrow \mathrm{OOH} + \mathrm{e}^- \tag{4}$$

$$\mathrm{OOH}^* + \mathrm{OH}^- \rightarrow * + \mathrm{O_2(g)} + \mathrm{H_2O(l)} + \mathrm{e}^- \tag{5}$$

The HER follows the mechanism:

$$* + \mathrm{H_2O(l)} + \mathrm{e}^- \rightarrow \mathrm{H}^* + \mathrm{OH}^- \quad \text{(Volmer step)} \tag{6}$$

$$2\mathrm{H}^* \rightarrow * + \mathrm{H_2} \quad \text{(Tafel step)} \tag{7}$$

$$\mathrm{H}^* + \mathrm{H_2O(l)} + \mathrm{e}^- \rightarrow * + \mathrm{H_2(g)} + \mathrm{OH}^- \quad \text{(Heyrovsky step)} \tag{8}$$

Here, the symbol * represents the adsorption site on the substrate. The Gibbs free energies for the OER and HER processes under alkaline conditions are given in the computational details section of the Supporting Information.

Acknowledgement

KM and MMM were supported by the Academy of Finland (grant # 338228). The computational resources were provided by the CSC–IT Center for Science, Espoo, Finland (`https://www.csc.fi/en/`) and the FGCI - Finnish Grid and Cloud Infrastructure. MA and AS were supported by the Research Office of the University of Kurdistan (Grant number 02-9-33926-135) and the Iranian Nanotechnology Initiative.

Supporting Information Available

Structural characterization detail of the samples, (Photo)Electrocatalytic performance, Computational details, Performance comparisons

References

(1) Chen, F.-Y.; Wu, Z.-Y.; Adler, Z.; Wang, H. Stability challenges of electrocatalytic oxygen evolution reaction: From mechanistic understanding to reactor design. *Joule* **2021**, *5*, 1704–1731.

(2) Osman, A. I.; Mehta, N.; Elgarahy, A. M.; Hefny, M.; Al-Hinai, A.; Al-Muhtaseb, A. H.; Rooney, D. W. Hydrogen production, storage, utilisation and environmental impacts: a review. *Environmental Chemistry Letters* **2022**, 1–36.

(3) Jiang, H.; Yu, Y.; Duan, X.; Chen, P.; Wang, S.; Qiu, X.; Ye, L.; Tu, X. Heterostructured MoO3 Anchored Defect-Rich NiFe-LDH/NF as a Robust Self-Supporting Electrocatalyst for Overall Water Splitting. *Small* **2023**, 2307797.

(4) Ji, X.; Lin, Y.; Zeng, J.; Ren, Z.; Lin, Z.; Mu, Y.; Qiu, Y.; Yu, J. Graphene/MoS2/FeCoNi (OH) x and Graphene/MoS2/FeCoNiPx multilayer-stacked vertical nanosheets on carbon fibers for highly efficient overall water splitting. *Nature Communications* **2021**, *12*, 1380.

(5) Liu, Z.-Q.; Liang, X.; Ma, F.-X.; Xiong, Y.-X.; Zhang, G.; Chen, G.; Zhen, L.; Xu, C.-Y. Decoration of NiFe-LDH Nanodots Endows Lower Fe-d Band Center of Fe1-N-C

Hollow Nanorods as Bifunctional Oxygen Electrocatalysts with Small Overpotential Gap. *Advanced Energy Materials* **2023**, *13*, 2203609.

(6) Mehdi, M.; An, B.-S.; Kim, H.; Lee, S.; Lee, C.; Seo, M.; Noh, M. W.; Cho, W.-C.; Kim, C.-H.; Choi, C. H.; others Rational Design of a Stable Fe-rich Ni-Fe Layered Double Hydroxide for the Industrially Relevant Dynamic Operation of Alkaline Water Electrolyzers. *Advanced Energy Materials* **2023**, *13*, 2204403.

(7) Lu, B.; Wahl, C. B.; Lu, X. K.; Sweers, M. E.; Li, H.; Dravid, V. P.; Seitz, L. C. Iridium-incorporated strontium tungsten oxynitride perovskite for efficient acidic hydrogen evolution. *Journal of the American Chemical Society* **2022**, *144*, 13547–13555.

(8) Yu, Y.; Lee, S. J.; Theerthagiri, J.; Lee, Y.; Choi, M. Y. Architecting the AuPt alloys for hydrazine oxidation as an anolyte in fuel cell: Comparative analysis of hydrazine splitting and water splitting for energy-saving H2 generation. *Applied Catalysis B: Environmental* **2022**, *316*, 121603.

(9) Shankar Naik, S.; Theerthagiri, J.; Nogueira, F. S.; Lee, S. J.; Min, A.; Kim, G.-A.; Maia, G.; Pinto, L. M.; Choi, M. Y. Dual-cation-coordinated CoFe-layered double-hydroxide nanosheets using the pulsed laser ablation technique for efficient electrochemical water splitting: mechanistic screening by in situ/operando raman and density functional theory calculations. *ACS Catalysis* **2023**, *13*, 1477–1491.

(10) Chen, C.; Tuo, Y.; Lu, Q.; Lu, H.; Zhang, S.; Zhou, Y.; Zhang, J.; Liu, Z.; Kang, Z.; Feng, X.; others Hierarchical trimetallic Co-Ni-Fe oxides derived from core-shell structured metal-organic frameworks for highly efficient oxygen evolution reaction. *Applied Catalysis B: Environmental* **2021**, *287*, 119953.

(11) Wang, H.; Wang, J.; Pi, Y.; Shao, Q.; Tan, Y.; Huang, X. Double Perovskite LaFexNi1-xO3 nanorods enable efficient oxygen evolution electrocatalysis. *Angewandte Chemie* **2019**, *131*, 2338–2342.

(12) Li, Y.; Yin, Z.; Cui, M.; Liu, X.; Xiong, J.; Chen, S.; Ma, T. Interface engineering of transitional metal sulfide–MoS 2 heterostructure composites as effective electrocatalysts for water-splitting. *Journal of Materials Chemistry A* **2021**, *9*, 2070–2092.

(13) Qian, Y.; Yu, J.; Zhang, Y.; Zhang, F.; Kang, Y.; Su, C.; Shi, H.; Kang, D. J.; Pang, H. Interfacial microenvironment modulation enhancing catalytic kinetics of binary metal sulfides heterostructures for advanced water splitting electrocatalysts. *Small Methods* **2022**, *6*, 2101186.

(14) Esswein, A. J.; Surendranath, Y.; Reece, S. Y.; Nocera, D. G. Highly active cobalt phosphate and borate based oxygen evolving catalysts operating in neutral and natural waters. *Energy & Environmental Science* **2011**, *4*, 499–504.

(15) Zou, X.; Zhang, W.; Zhou, X.; Song, K.; Ge, X.; Zheng, W. The surface of metal boride tinted by oxygen evolution reaction for enhanced water electrolysis. *Journal of Energy Chemistry* **2022**, *72*, 509–515.

(16) Lyu, C.; Cheng, J.; Wu, K.; Wu, J.; Wang, N.; Guo, Z.; Hu, P.; Lau, W.-M.; Zheng, J. Interfacial electronic structure modulation of CoP nanowires with FeP nanosheets for enhanced hydrogen evolution under alkaline water/seawater electrolytes. *Applied Catalysis B: Environmental* **2022**, *317*, 121799.

(17) Sun, H.; Min, Y.; Yang, W.; Lian, Y.; Lin, L.; Feng, K.; Deng, Z.; Chen, M.; Zhong, J.; Xu, L.; others Morphological and electronic tuning of Ni2P through iron doping toward highly efficient water splitting. *ACS Catalysis* **2019**, *9*, 8882–8892.

(18) Feng, M.; Huang, J.; Peng, Y.; Huang, C.; Yue, X.; Huang, S. Tuning electronic structures of transition metal carbides to boost oxygen evolution reactions in acidic medium. *ACS nano* **2022**, *16*, 13834–13844.

(19) Gu, Y.; Wei, B.; Legut, D.; Fu, Z.; Du, S.; Zhang, H.; Francisco, J. S.; Zhang, R. Sin-

gle Atom-Modified Hybrid Transition Metal Carbides as Efficient Hydrogen Evolution Reaction Catalysts. *Advanced Functional Materials* **2021**, *31*, 2104285.

(20) Hu, H.; Zhang, Z.; Zhang, Y.; Thomas, T.; Du, H.; Huang, K.; Attfield, J. P.; Yang, M. An ultra-low Pt metal nitride electrocatalyst for sustainable seawater hydrogen production. *Energy & Environmental Science* **2023**, *16*, 4584–4592.

(21) Jin, H.; Wang, X.; Tang, C.; Vasileff, A.; Li, L.; Slattery, A.; Qiao, S.-Z. Stable and highly efficient hydrogen evolution from seawater enabled by an unsaturated nickel surface nitride. *Advanced Materials* **2021**, *33*, 2007508.

(22) Zhong, H.; Wang, M.; Chen, G.; Dong, R.; Feng, X. Two-dimensional conjugated metal–organic frameworks for electrocatalysis: opportunities and challenges. *ACS nano* **2022**, *16*, 1759–1780.

(23) Naghshbandi, Z.; Moradi, K.; Salimi, A.; Gholinejad, M.; Feizabadi, A. Multi metallic Electro-Catalyst Design for Enhanced Oxygen Evolution Reaction: Immobilizing MnFe Nanoparticles on ZIF-67-decorated Graphene Oxide. *Electrochimica Acta* **2024**, 143884.

(24) Cao, J.; Mou, T.; Mei, B.; Yao, P.; Han, C.; Gong, X.; Song, P.; Jiang, Z.; Frauenheim, T.; Xiao, J.; others Improved Electrocatalytic Activity and Stability by Single Iridium Atoms on Iron-based Layered Double Hydroxides for Oxygen Evolution. *Angewandte Chemie* **2023**, *135*, e202310973.

(25) Zhou, Y.; Fan, H. J. Progress and challenge of amorphous catalysts for electrochemical water splitting. *ACS Materials Letters* **2020**, *3*, 136–147.

(26) Jia, B.; Liu, G.; Zhang, B.; Zheng, J.; Yin, K.; Lin, J.; Han, C.; Fan, X.; Xu, M.; Ye, L. General Modification Strategy on Amorphous Materials to Boost Catalytic Performance. *Advanced Functional Materials* **2024**, *n/a*, 2405867.

(27) Boumeriame, H.; Da Silva, E. S.; Cherevan, A. S.; Chafik, T.; Faria, J. L.; Eder, D. Layered double hydroxide (LDH)-based materials: A mini-review on strategies to improve the performance for photocatalytic water splitting. *Journal of Energy Chemistry* **2022**, *64*, 406–431.

(28) Moloudi, M.; Noori, A.; Rahmanifar, M. S.; Shabangoli, Y.; El-Kady, M. F.; Mohamed, N. B.; Kaner, R. B.; Mousavi, M. F. Layered Double Hydroxide Templated Synthesis of Amorphous NiCoFeB as a Multifunctional Electrocatalyst for Overall Water Splitting and Rechargeable Zinc–Air Batteries. *Advanced Energy Materials* **2023**, *13*, 2203002.

(29) Bao, W.; Tang, Y.; Yu, J.; Yan, W.; Wang, C.; Li, Y.; Wang, Z.; Yang, J.; Zhang, L.; Yu, F. Si-doped ZnAl-LDH nanosheets by layer-engineering for efficient photoelectrocatalytic water splitting. *Applied Catalysis B: Environment and Energy* **2024**, *346*, 123706.

(30) Lv, J.; Wang, L.; Li, R.; Zhang, K.; Zhao, D.; Li, Y.; Li, X.; Huang, X.; Wang, G. Constructing a hetero-interface composed of oxygen vacancy-enriched Co3O4 and crystalline–amorphous NiFe-LDH for oxygen evolution reaction. *ACS Catalysis* **2021**, *11*, 14338–14351.

(31) Guo, X.; Zheng, X.; Hu, X.; Zhao, Q.; Li, L.; Yu, P.; Jing, C.; Zhang, Y.; Huang, G.; Jiang, B.; others Electrostatic adsorbing graphene quantum dot into nickel–based layered double hydroxides: Electron absorption/donor effects enhanced oxygen electrocatalytic activity. *Nano Energy* **2021**, *84*, 105932.

(32) Wang, Y.; Zhang, Y.; Liu, Z.; Xie, C.; Feng, S.; Liu, D.; Shao, M.; Wang, S. Layered double hydroxide nanosheets with multiple vacancies obtained by dry exfoliation as highly efficient oxygen evolution electrocatalysts. *Angewandte Chemie International Edition* **2017**, *56*, 5867–5871.

(33) Kim, M. S.; Lamichhane, B.; Lee, J.-H.; Bae, J.-G.; Heo, J. Y.; Lee, H. J.; Kattel, S.; Lee, J. H. Identification and comparison of the local physicochemical structures of transition metal-based layered double hydroxides for high performance electrochemical oxygen evolution reactions. *Journal of Energy Chemistry* **2023**, *87*, 89–97.

(34) Zheng, Z.; Wu, D.; Chen, L.; Chen, S.; Wan, H.; Chen, G.; Zhang, N.; Liu, X.; Ma, R. Collaborative optimization of thermodynamic and kinetic for Ni-based hydroxides in electrocatalytic urea oxidation reaction. *Applied Catalysis B: Environmental* **2024**, *340*, 123214.

(35) Qiu, Z.; Tai, C.-W.; Niklasson, G. A.; Edvinsson, T. Direct observation of active catalyst surface phases and the effect of dynamic self-optimization in NiFe-layered double hydroxides for alkaline water splitting. *Energy & Environmental Science* **2019**, *12*, 572–581.

(36) Zhang, J.; Liu, J.; Xi, L.; Yu, Y.; Chen, N.; Sun, S.; Wang, W.; Lange, K. M.; Zhang, B. Single-atom Au/NiFe layered double hydroxide electrocatalyst: probing the origin of activity for oxygen evolution reaction. *Journal of the American Chemical Society* **2018**, *140*, 3876–3879.

(37) He, X.; Han, X.; Zhou, X.; Chen, J.; Wang, J.; Chen, Y.; Yu, L.; Zhang, N.; Li, J.; Wang, S.; others Electronic modulation with Pt-incorporated NiFe layered double hydroxide for ultrastable overall water splitting at 1000 mA cm- 2. *Applied Catalysis B: Environmental* **2023**, *331*, 122683.

(38) Lv, L.; Yang, Z.; Chen, K.; Wang, C.; Xiong, Y. 2D layered double hydroxides for oxygen evolution reaction: from fundamental design to application. *Advanced Energy Materials* **2019**, *9*, 1803358.

(39) Yu, J.; Yu, F.; Yuen, M.-F.; Wang, C. Two-dimensional layered double hydroxides as a

platform for electrocatalytic oxygen evolution. *Journal of Materials Chemistry A* **2021**, *9*, 9389–9430.

(40) Yan, D.; Li, Y.; Huo, J.; Chen, R.; Dai, L.; Wang, S. Defect chemistry of nonprecious-metal electrocatalysts for oxygen reactions. *Advanced materials* **2017**, *29*, 1606459.

(41) Hui, L.; Xue, Y.; Huang, B.; Yu, H.; Zhang, C.; Zhang, D.; Jia, D.; Zhao, Y.; Li, Y.; Liu, H.; others Overall water splitting by graphdiyne-exfoliated and-sandwiched layered double-hydroxide nanosheet arrays. *Nature communications* **2018**, *9*, 5309.

(42) Zhang, R.; Zhang, Y.-C.; Pan, L.; Shen, G.-Q.; Mahmood, N.; Ma, Y.-H.; Shi, Y.; Jia, W.; Wang, L.; Zhang, X.; others Engineering cobalt defects in cobalt oxide for highly efficient electrocatalytic oxygen evolution. *Acs Catalysis* **2018**, *8*, 3803–3811.

(43) Ma, T. Y.; Dai, S.; Jaroniec, M.; Qiao, S. Z. Metal–organic framework derived hybrid Co3O4-carbon porous nanowire arrays as reversible oxygen evolution electrodes. *Journal of the American Chemical Society* **2014**, *136*, 13925–13931.

(44) Sha, L.; Liu, T.; Ye, K.; Zhu, K.; Yan, J.; Yin, J.; Wang, G.; Cao, D. A heterogeneous interface on NiS@ Ni 3 S 2/NiMoO 4 heterostructures for efficient urea electrolysis. *Journal of Materials Chemistry A* **2020**, *8*, 18055–18063.

(45) Oh, N. K.; Seo, J.; Lee, S.; Kim, H.-J.; Kim, U.; Lee, J.; Han, Y.-K.; Park, H. Highly efficient and robust noble-metal free bifunctional water electrolysis catalyst achieved via complementary charge transfer. *Nature Communications* **2021**, *12*, 4606.

(46) Huang, H.; Ning, S.; Xie, Y.; He, Z.; Teng, J.; Chen, Z.; Fan, Y.; Shi, J.-Y.; Barboiu, M.; Wang, D.; others Synergistic Modulation of Electronic Interaction to Enhance Intrinsic Activity and Conductivity of Fe–Co–Ni Hydroxide Nanotube for Highly Efficient Oxygen Evolution Electrocatalyst. *Small* **2023**, 2302272.

(47) Huo, J.-M.; Wang, Y.; Xue, J.-N.; Yuan, W.-Y.; Zhai, Q.-G.; Hu, M.-C.; Li, S.-N.; Chen, Y. High-Valence Metal Doping Induced Lattice Expansion for M-FeNi LDH toward Enhanced Urea Oxidation Electrocatalytic Activities. *Small* **2024**, *20*, 2305877.

(48) Karmakar, A.; Karthick, K.; Sankar, S. S.; Kumaravel, S.; Madhu, R.; Kundu, S. A vast exploration of improvising synthetic strategies for enhancing the OER kinetics of LDH structures: a review. *Journal of Materials Chemistry A* **2021**, *9*, 1314–1352.

(49) Zhou, D.; Li, P.; Lin, X.; McKinley, A.; Kuang, Y.; Liu, W.; Lin, W.-F.; Sun, X.; Duan, X. Layered double hydroxide-based electrocatalysts for the oxygen evolution reaction: identification and tailoring of active sites, and superaerophobic nanoarray electrode assembly. *Chemical Society Reviews* **2021**, *50*, 8790–8817.

(50) Lei, H.; Wan, Q.; Tan, S.; Wang, Z.; Mai, W. Pt-Quantum-Dot-Modified Sulfur-Doped NiFe Layered Double Hydroxide for High-Current-Density Alkaline Water Splitting at Industrial Temperature. *Advanced Materials* **2023**, *35*, 2208209.

(51) Zheng, L.; Teng, F.; Ye, X.; Zheng, H.; Fang, X. Photo/electrochemical applications of metal sulfide/TiO2 heterostructures. *Advanced Energy Materials* **2020**, *10*, 1902355.

(52) Lu, X.; Xue, H.; Gong, H.; Bai, M.; Tang, D.; Ma, R.; Sasaki, T. 2D layered double hydroxide nanosheets and their derivatives toward efficient oxygen evolution reaction. *Nano-Micro Letters* **2020**, *12*, 1–32.

(53) Wang, S.; Ning, X.; Cao, Y.; Chen, R.; Lu, Z.; Hu, J.; Xie, J.; Hao, A. Construction of an advanced NiFe-LDH/MoS2–Ni3S2/NF heterostructure catalyst toward efficient electrocatalytic overall water splitting. *Inorganic Chemistry* **2023**, *62*, 6428–6438.

(54) Cao, N.; Di, Y.; Chen, S.; Jin, X.; Liu, M.; Shao, Q.; Zang, X. Hierarchical nanoarchitecture with NiFe-LDH on MoS2 for enhanced electrocatalysis of hydrogen evolution in alkaline media. *Electrochimica Acta* **2023**, *467*, 143079.

(55) Liu, Y.; Zhang, H.; Ke, J.; Zhang, J.; Tian, W.; Xu, X.; Duan, X.; Sun, H.; Tade, M. O.; Wang, S. 0D (MoS2)/2D (g-C3N4) heterojunctions in Z-scheme for enhanced photocatalytic and electrochemical hydrogen evolution. *Applied Catalysis B: Environmental* **2018**, *228*, 64–74.

(56) Hu, Z.; Wu, Z.; Han, C.; He, J.; Ni, Z.; Chen, W. Two-dimensional transition metal dichalcogenides: interface and defect engineering. *Chemical Society Reviews* **2018**, *47*, 3100–3128.

(57) Acerce, M.; Akdoğan, E. K.; Chhowalla, M. Metallic molybdenum disulfide nanosheet-based electrochemical actuators. *Nature* **2017**, *549*, 370–373.

(58) Chen, B.; Hu, P.; Yang, F.; Hua, X.; Yang, F. F.; Zhu, F.; Sun, R.; Hao, K.; Wang, K.; Yin, Z. In situ porousized MoS2 nano islands enhance HER/OER bifunctional electrocatalysis. *Small* **2023**, *19*, 2207177.

(59) Ren, X.; Pang, L.; Zhang, Y.; Ren, X.; Fan, H.; Liu, S. F. One-step hydrothermal synthesis of monolayer MoS 2 quantum dots for highly efficient electrocatalytic hydrogen evolution. *Journal of Materials Chemistry A* **2015**, *3*, 10693–10697.

(60) Yu, Y.; Ma, T.; Huang, H. Semiconducting Quantum Dots for Energy Conversion and Storage. *Advanced Functional Materials* **2023**, 2213770.

(61) Ou, G.; Fan, P.; Ke, X.; Xu, Y.; Huang, K.; Wei, H.; Yu, W.; Zhang, H.; Zhong, M.; Wu, H.; others Defective molybdenum sulfide quantum dots as highly active hydrogen evolution electrocatalysts. *Nano Research* **2018**, *11*, 751–761.

(62) Li, X.; Lv, X.; Li, N.; Wu, J.; Zheng, Y.-Z.; Tao, X. One-step hydrothermal synthesis of high-percentage 1T-phase MoS2 quantum dots for remarkably enhanced visible-light-driven photocatalytic H2 evolution. *Applied Catalysis B: Environmental* **2019**, *243*, 76–85.

(63) Mohanty, B.; Ghorbani-Asl, M.; Kretschmer, S.; Ghosh, A.; Guha, P.; Panda, S. K.; Jena, B.; Krasheninnikov, A. V.; Jena, B. K. MoS2 quantum dots as efficient catalyst materials for the oxygen evolution reaction. *Acs Catalysis* **2018**, *8*, 1683–1689.

(64) Vikraman, D.; Akbar, K.; Hussain, S.; Yoo, G.; Jang, J.-Y.; Chun, S.-H.; Jung, J.; Park, H. J. Direct synthesis of thickness-tunable MoS2 quantum dot thin layers: Optical, structural and electrical properties and their application to hydrogen evolution. *Nano Energy* **2017**, *35*, 101–114.

(65) Yousefzadeh, H.; Noori, A.; Rahmanifar, M. S.; Hassani, N.; Neek-Amal, M.; El-Kady, M. F.; Vinu, A.; Kaner, R. B.; Mousavi, M. F. Partial sulfidation of the electrochemically exfoliated layered double hydroxides toward advanced aqueous zinc batteries. *Advanced Energy Materials* **2023**, *13*, 2302137.

(66) Zhang, M.; Liu, Y.; Liu, B.; Chen, Z.; Xu, H.; Yan, K. Trimetallic NiCoFe-layered double hydroxides nanosheets efficient for oxygen evolution and highly selective oxidation of biomass-derived 5-hydroxymethylfurfural. *Acs Catalysis* **2020**, *10*, 5179–5189.

(67) Liao, F.; Yang, G.; Cheng, Q.; Mao, L.; Zhao, X.; Chen, L. Rational design and facile synthesis of Ni-Co-Fe ternary LDH porous sheets for high-performance aqueous asymmetric supercapacitor. *Electrochimica Acta* **2022**, *428*, 140939.

(68) Gao, X.; Yu, Y.; Liang, Q.; Pang, Y.; Miao, L.; Liu, X.; Kou, Z.; He, J.; Pennycook, S. J.; Mu, S.; others Surface nitridation of nickel-cobalt alloy nanocactoids raises the performance of water oxidation and splitting. *Applied Catalysis B: Environmental* **2020**, *270*, 118889.

(69) Liu, D.; Ai, H.; Li, J.; Fang, M.; Chen, M.; Liu, D.; Du, X.; Zhou, P.; Li, F.; Lo, K. H.; others Surface reconstruction and phase transition on vanadium–cobalt–iron trimetal nitrides to form active oxyhydroxide for enhanced electrocatalytic water oxidation. *Advanced Energy Materials* **2020**, *10*, 2002464.

(70) Liang, C.; Zou, P.; Nairan, A.; Zhang, Y.; Liu, J.; Liu, K.; Hu, S.; Kang, F.; Fan, H. J.; Yang, C. Exceptional performance of hierarchical Ni–Fe oxyhydroxide@ NiFe alloy nanowire array electrocatalysts for large current density water splitting. *Energy & Environmental Science* **2020**, *13*, 86–95.

(71) Yuan, W.; Wang, S.; Ma, Y.; Qiu, Y.; An, Y.; Cheng, L. Interfacial engineering of cobalt nitrides and mesoporous nitrogen-doped carbon: toward efficient overall water-splitting activity with enhanced charge-transfer efficiency. *ACS Energy Letters* **2020**, *5*, 692–700.

(72) Liang, Q.; Jin, H.; Wang, Z.; Xiong, Y.; Yuan, S.; Zeng, X.; He, D.; Mu, S. Metal-organic frameworks derived reverse-encapsulation Co-NC@ Mo2C complex for efficient overall water splitting. *Nano Energy* **2019**, *57*, 746–752.

(73) Song, F.; Li, W.; Yang, J.; Han, G.; Yan, T.; Liu, X.; Rao, Y.; Liao, P.; Cao, Z.; Sun, Y. Interfacial sites between cobalt nitride and cobalt act as bifunctional catalysts for hydrogen electrochemistry. *ACS Energy Letters* **2019**, *4*, 1594–1601.

(74) Li, H.; Chen, S.; Zhang, Y.; Zhang, Q.; Jia, X.; Zhang, Q.; Gu, L.; Sun, X.; Song, L.; Wang, X. Systematic design of superaerophobic nanotube-array electrode comprised of transition-metal sulfides for overall water splitting. *Nature communications* **2018**, *9*, 2452.

(75) Gupta, S.; Patel, N.; Fernandes, R.; Kadrekar, R.; Dashora, A.; Yadav, A.; Bhattacharyya, D.; Jha, S.; Miotello, A.; Kothari, D. Co–Ni–B nanocatalyst for efficient hydrogen evolution reaction in wide pH range. *Applied Catalysis B: Environmental* **2016**, *192*, 126–133.

(76) Yu, Z.-Y.; Lang, C.-C.; Gao, M.-R.; Chen, Y.; Fu, Q.-Q.; Duan, Y.; Yu, S.-H. Ni–Mo–O nanorod-derived composite catalysts for efficient alkaline water-to-hydrogen conversion via urea electrolysis. *Energy & Environmental Science* **2018**, *11*, 1890–1897.

(77) Eda, G.; Yamaguchi, H.; Voiry, D.; Fujita, T.; Chen, M.; Chhowalla, M. Photoluminescence from chemically exfoliated MoS2. *Nano letters* **2011**, *11*, 5111–5116.

(78) Zhai, P.; Xia, M.; Wu, Y.; Zhang, G.; Gao, J.; Zhang, B.; Cao, S.; Zhang, Y.; Li, Z.; Fan, Z.; others Engineering single-atomic ruthenium catalytic sites on defective nickel-iron layered double hydroxide for overall water splitting. *Nature Communications* **2021**, *12*, 4587.

(79) Shinagawa, T.; Garcia-Esparza, A. T.; Takanabe, K. Insight on Tafel slopes from a microkinetic analysis of aqueous electrocatalysis for energy conversion. *Scientific Reports* **2015**, *5*, 13801.

(80) Zhou, J.; Yu, L.; Zhu, Q.; Huang, C.; Yu, Y. Defective and ultrathin NiFe LDH nanosheets decorated on V-doped Ni 3 S 2 nanorod arrays: a 3D core–shell electrocatalyst for efficient water oxidation. *Journal of Materials Chemistry A* **2019**, *7*, 18118–18125.

(81) Yang, W.; Yang, X.; Li, B.; Lin, J.; Gao, H.; Hou, C.; Luo, X. Ultrathin nickel hydroxide nanosheets with a porous structure for efficient electrocatalytic urea oxidation. *Journal of materials chemistry A* **2019**, *7*, 26364–26370.

(82) Nørskov, J. K.; Rossmeisl, J.; Logadottir, A.; Lindqvist, L.; Kitchin, J. R.; Bligaard, T.; Jonsson, H. Origin of the overpotential for oxygen reduction at a fuel-cell cathode. *The Journal of Physical Chemistry B* **2004**, *108*, 17886–17892.

(83) Exner, K. S. Hydrogen electrocatalysis revisited: Weak bonding of adsorbed hydrogen as the design principle for active electrode materials. *Current Opinion in Electrochemistry* **2021**, *26*, 100673.

(84) Wang, Z.; Goddard, W. A.; Xiao, H. Potential-dependent transition of reaction mechanisms for oxygen evolution on layered double hydroxides. *Nature Communications* **2023**, *14*, 4228.

(85) Binninger, T.; Kowalski, P. M.; Eikerling, M. H. Oxygen desorption–Critical step for the oxygen evolution reaction. *Current Opinion in Electrochemistry* **2023**, 101382.

(86) Mortensen, J. J.; Larsen, A. H.; Kuisma, M.; Ivanov, A. V.; Taghizadeh, A.; Peterson, A.; Haldar, A.; Dohn, A. O.; Schäfer, C.; Jónsson, E. Ö.; others GPAW: An open Python package for electronic structure calculations. *The Journal of Chemical Physics* **2024**, *160*.

(87) Blöchl, P. E. Projector augmented-wave method. *Physical review B* **1994**, *50*, 17953.

(88) Perdew, J. P.; Burke, K.; Ernzerhof, M. Generalized gradient approximation made simple. *Physical review letters* **1996**, *77*, 3865.

(89) Tripkovic, V.; Hansen, H. A.; Vegge, T. From 3D to 2D Co and Ni oxyhydroxide catalysts: Elucidation of the active site and influence of doping on the oxygen evolution activity. *ACS Catalysis* **2017**, *7*, 8558–8571.

(90) Goldsmith, Z. K.; Harshan, A. K.; Gerken, J. B.; Vörös, M.; Galli, G.; Stahl, S. S.; Hammes-Schiffer, S. Characterization of NiFe oxyhydroxide electrocatalysts by integrated electronic structure calculations and spectroelectrochemistry. *Proceedings of the National Academy of Sciences* **2017**, *114*, 3050–3055.

(91) Gao, Y.; Liu, B.; Wang, D. Microenvironment engineering of single/dual-atom catalysts for electrocatalytic application. *Advanced Materials* **2023**, *35*, 2209654.